Original Research Article

Quality and Image Processing Analysis versus Radiation Dose in Hip Radiographic Examinations

.

ABSTRACT

SAMPLE ABSTRACT:

Aims: This study addressed the evaluation of image quality and processing in hip radiographic examinations

Study design: Exploring six combinations of exposure techniques commonly used in clinical practice. These techniques maintained constant voltage (kVp) while varying only the current/time (mA.s).

Place and Duration of Study: The study was carried out at the Radiodiagnosis Laboratory of the Radiology and Medical Physics undergraduate courses at the Franciscan University (UFN), as part of the research developed during the Image Processing course in the second semester of 2023.

Methodology: Image acquisition and radiation dose measurement were performed using clinical radiographic equipment and a model resembling hip anatomy, along with a dosimetric system to quantify radiation dose at the entrance surface (ESAK). The captured images were digitized through a computerized radiography (CR) system, enabling quantitative analysis using histograms and Regions of Interest (ROI) in anatomical structures relevant for diagnosis. Signal and noise values were evaluated, allowing the determination of the signal-to-noise ratio (SNR) and radiographic contrast (CR).

Results: The results revealed significant differences among the various techniques employed. Some images displayed lower SNR, ranging from 8.14% to 15.60%, yet with higher CR, varying between 5.48% and 22.29%. Remarkably, one technique (70 kVp with 16 mA.s) demonstrated the best cost-benefit relationship, reducing radiation exposure by 48.7% (from 6.32 to 3.24 mGy) with minimal reduction in SNR, less than 10%, and a 5.47% increase in CR.

Conclusion: These findings underscore the importance for radiology professionals to seek imaging techniques ensuring high diagnostic quality with minimal patient exposure. Prioritizing safer and more effective radiological practices is essential for delivering quality healthcare services.

Keywords: [Radiographic examination, Hip, Computer-Assisted Image Processing, Signal-to-Noise Ratio]

1. INTRODUCTION

Digital image processing involves the systematic application of highly complex mathematical algorithms aimed at manipulating images obtained through computerized radiology systems [1]. Presently, computerized radiology systems are widely employed in practice for image processing in radiographic exams.

Computerized radiology systems rely on photo-stimulable phosphors, known as trapping phosphors, often in the form of barium fluorohalides (BaFl), deposited on an imaging plate (IP). In the computerized radiology system, X-ray absorption differs from the screen-film system as light emission occurs after the formation of the latent image, where trapped charges are stimulated and released from metastable traps to generate the digital image (ID) [2]. The ID results from the interpretation of the Imaging Plate (IP) and the application of computational algorithms to the original data obtained by the computerized radiology system, then displayed on the workstation monitor [2,3].

Further studies by Erenstein et al. [4] note that reducing the radiation dose at the patient's skin surface entrance (Entrance Skin Air Kerma - ESAK) during the acquisition of radiographic images can compromise image quality (IQ) and vice versa. However, Digital Systems (DS) have the ability to electronically present radiographic contrast, adapting to various exposure settings. This brightness control is achieved through software employing predefined digital processing algorithms. Although what limits IQ is noise, i.e., the standard deviation between pixel values in the ID [3,4].

According to Furquim and Costa [5], medical images are formatted in the DICOM (Digital Imaging and Communications in Medicine) protocol, together with their associated data, stored in an image management system known as PACS (Picture Archiving and Communication System). DICOM enables secure and effective transmission of images between different systems, while PACS keeps the images organized and accessible to physicians.

The use of open-source software, ImageJ, has proven to be an important tool for evaluating the quality and processing of medical images, offering robust tools for precise image analysis. By using ImageJ, radiology professionals have the ability to perform detailed measurements, contrast adjustments, calibration, and statistical analysis of medical images. This not only enhances diagnostic accuracy but also contributes to radiology research and development [3-6].

Studies by Flinthan et al. [7] and Trozic; England; Mekis [8] emphasized that hip radiographic examination is one of the most frequent procedures in clinical practice. Additionally, studies by Yoneda; Fujii; Tanaka [9] identified that this anatomy houses part of the bone marrow (blood cells) and germ cells (gonads), which are sensitive to radiation in the human body. Thus, this study aims to evaluate the quality and image processing using tools from the ImageJ software for computerized radiology systems in hip radiographic exams.

Antero-posterior (AP) Radiographic Examination of the Hip

The radiographic positioning for hip exams may vary depending on the desired study type and the patient's clinical conditions [10]. During the general positioning of the patient for hip exams, the patient should lie supine (on their back) on the examination table, the lower limb to be examined is fully extended, and the foot of the extended limb is internally rotated by about 15-20 degrees. The X-ray beam is directed perpendicularly to the hip region, centered at the midpoint between the iliac crest and the pubic symphysis, as depicted in Figure 1.

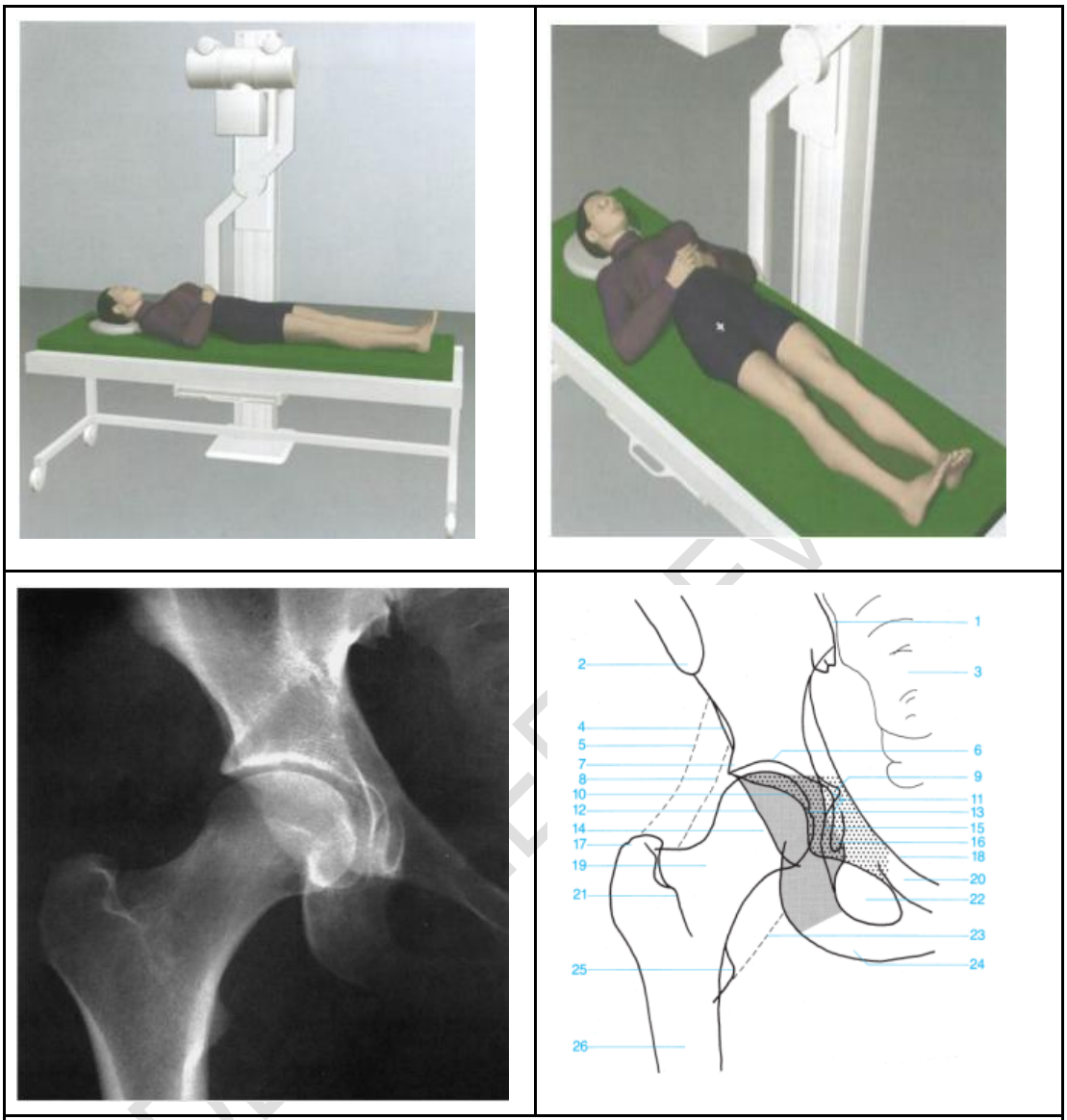

In the illustration, the enumerated anatomical landmarks represent: 1 - Sacroiliac joint, 2 - Lower anterior iliac spine, 3 - Sacrum, 4 - Lower anterior iliac spine, 5 - Fat stripes (between gluteal muscles), 6 - Upper part (ceiling) of the hip joint, 7 - Acetabulum, 8 - Fat stripes (medially to the gluteus minimus muscle), 9 - Ischial spine, 10 - Anterior margin of the joint cavity, 11 - Medial part (floor) of the joint cavity, 12 - Posterior margin of the joint cavity, 13 - Fovea of the femoral head, 14 - Femoral head, 15 - Ischial line, 16 - Tear-shaped image (Köhler's teardrop), 17 - Greater trochanter, 18 - Terminal line, 19 - Femoral neck, 20 - Superior ramus of the pubic bone, 21 - Intertrochanteric crest (medially to the gluteus minimus muscle), 22 - Obturator foramen, 23 - Fat stripe (medially to the psoas muscle), 24 - Ischial tuberosity, 25 - Lesser trochanter, 26 - Femur.

Fig. 1 - Image composition during the examination/hip anatomy.
Source: Illustrations of positioning by Sandström; Pettersson; Åkerman [11] (P.87, 2003) and Radiography and radiological anatomy of the hip adapted from Möller [12] (P.156 and 157, 2000).

However, in specific clinical situations, additional oblique projections or special incidences might be necessary to better evaluate certain anatomical structures or pathologies. It's important for these examinations to be performed by trained radiology professionals to ensure image quality and accurate assessment.

2. MATERIAL AND METHODS

The study was conducted at the Radiodiagnosis Laboratory of the undergraduate courses in Radiology and Medical Physics as part of the research developed during the Image Processing discipline at the Franciscan University (UFN).
A semi-anatomical phantom was used for the measurements, which was developed by students from the Medical Physics course at UFN. The Phantom consists of a basic internal part, a bony skeleton (lumbar spine and bilateral hip - pelvis), and an external part, an acrylic resin of thickness equivalent to a typical adult, which covers the skeleton. The phantom was chosen due to the techniques used for obtaining an image, being the same techniques applied for imaging a human hip in a radiographic examination, in addition to reproducing densities close to a human hip, making the assay very similar to a real examination.
In this study, an Intecal X-ray equipment, model MAAF, operated with a high-frequency generator, was used. The broad focal spot (1.2 mm^2) was chosen as suitable for hip examinations. Images were obtained with a grid ratio of 10:1 (52 lines/cm) and a Source-to-Image-Distance (SID) of 1 meter in the cassette drawer (Figure 2). For the digital image capture, a CR system was employed, Carestream brand, consisting of a digitizer, workstation, and a 24 cm x 30 cm cassette, an Imaging Plate (IP), with a spatial resolution of 10 pixels/mm and a resolution scale of 16 bits/pixel. The images were viewed on the workstation monitor of the system. Radiation beam measurements were performed using a RADICAL dosimetric system, model 9015, calibrated in a reference laboratory. To quantify the images, a publicly available computer program, ImageJ, was used.

2.1 Methodology

2.1.1 Image Acquisition and Radiation Dose Measurement

During the image acquisition, a semi-anatomical hip phantom was used. The images were acquired using the same 24 cm x 30 cm cassette throughout the assay, centered to represent the hip examination/anatomy, placed on the table's bucky, avoiding variations in latent image acquisition, as illustrated in Figure 1.
Table 1 represents the values of the product of current by time (mA.s) selected on the control panel of the X-ray equipment, activated during image acquisition and radiation dose measurement. As suggested by Sandström; Pettersson; Åkerman [11] (P.87, 2003) from the Diagnostic Imaging Manual: Radiographic Technique and Projections of the World Health Organization, the voltage (kVp) and electric current were maintained constant at 200 mA. Figure 2 illustrates the geometry for image acquisition and radiation dose measurement.

Table 1. Electrical factors selected during image acquisition

Electrical Factors	Image 1	Image 2	Image 3	Image 4	Image 5	Image 6
kVp	70					
mA.s	10	12,6	16	20	25	32

Source: Author's own.

Image Acquisition **Entrance Skin air KERMA - ESAK**

Fig. 2. Geometry for Image Acquisition and Radiation Dose Measurement.
Source: Author's own.

Figure 2A illustrates the irradiation geometry for obtaining the phantom image, where the Source-to-Image-Distance (SID) is 100 cm, and the Source-to-Phantom-Surface Distance (SPSD) is 20 cm. Figure 2B illustrates the irradiation geometry for obtaining the dose. The sensitive area of the ionization chamber was positioned above the phantom to evaluate the dose at the surface.

2.1.2 Selection Criteria

All data were entered into Excel 2007 (Microsoft Corp, Washington, USA) to facilitate descriptive analysis. As there were no reference values to define the quality descriptors' limits, the values measured in the reference images acquired with 32 mA.s, as suggested by Sandström; Pettersson; Åkerman [11] (P.87, 2003), were considered 'reference' values. The percentage deviation (D%) was chosen to compare the acquired images with the reference image, following equation 1.

$$D(\%) = \left[\left(\frac{New\ \ value}{De\ fault\ \ \ value}\right) - 1 \times (100)\right] \quad (1)$$

2.1.3 Image Quality

The image quality was assessed using the open-source software ImageJ [6]. In this study, we conducted a quantitative evaluation using ImageJ software to obtain signal and noise values through histograms and regions of interest (ROI). We opted for analyzing the images in DICOM format.

3. RESULTS AND DISCUSSION

3.1 Histogram

Using the ImageJ program, we executed the radiographic images and used the shortcut Ctrl+H to generate each histogram. The histogram was displayed in a new window, with the X-axis representing pixel intensity values and the Y-axis representing the quantity of pixels with these values. Overall, each image presents an average signal value and standard deviation (noise) contained within it [6].
A histogram can be useful for visually assessing the spectrum and measurements on the graph, as well as quantifying each image's average signal and noise values overall. The overall analysis result of Image Quality obtained through the histogram of each image is represented in Figure 3.

Image 1

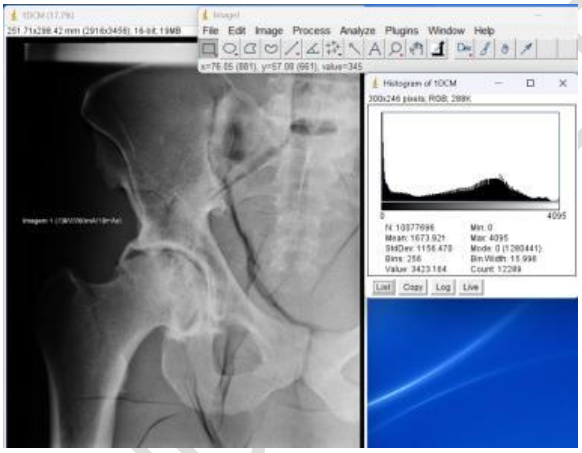

Image 2

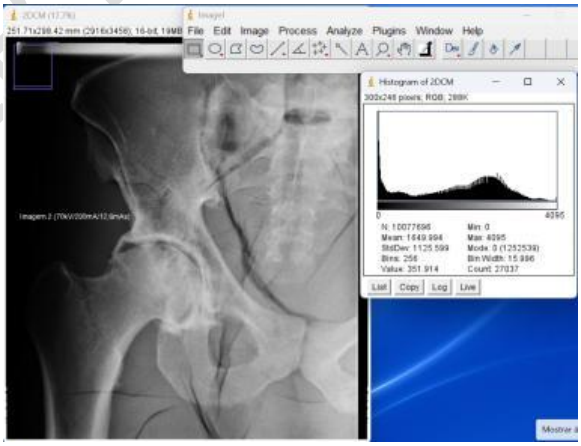

Image 3

Image 4

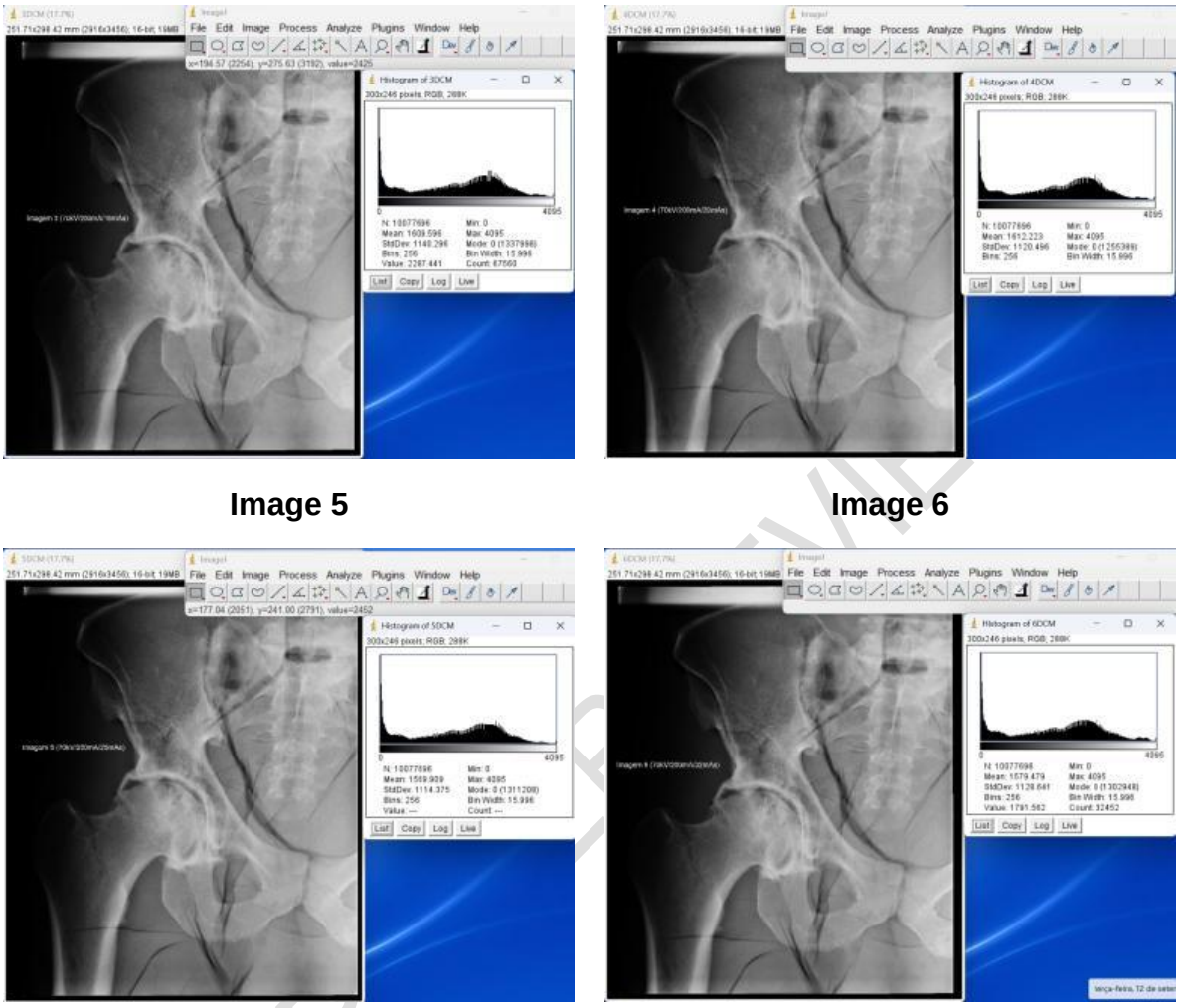

Fig. 3 - Shows the hip image and the respective image histogram for each technique.
Source: Author's own.

Table 2 represents the average signal and noise values along with their respective percentage deviations concerning Image 6.

Table 2. Relationship of exposure indicators and Image Quality (IQ) obtained from histograms.

Electrical Factors			IQ			
	kV	mAs	Signal	D%	Noise	D%
Image 1	70	10	1673,9	5,98%	1156,5	2,47%
Image 2		12,6	1650	4,46%	1125,6	-0,27%
Image 3		16	1609,6	1,91%	1140,3	1,04%

Image 4	20	1612,2	2,07%	1120,5	-0,72%
Image 5	25	1569,9	-0,61%	1114,4	-1,26%
Image 6	32	1579,5	Reference	1128,6	Reference

Source: Author's own.

Results from Table 2 provide a detailed analysis of average signal and noise values, comparing them with Image 6 as a reference. It's evident that different exposure techniques result in noticeable variations in signal and noise indicators. Some images show considerably higher signals, while others demonstrate slightly lower signals compared to Image 6. The percentage deviations highlight noise variations, indicating both decreases and increases concerning the reference, suggesting that variations in exposure techniques, especially kV and mAs, directly influence these indicators. Techniques with higher kV values tend to result in slightly higher signals, while changes in mAs have a more pronounced influence on noise. This analysis is crucial for assessing IQ in medical or scientific contexts, although the final interpretation should consider other aspects besides these indicators for a comprehensive evaluation of clinical or scientific imaging.

3.2 Signal and Noise Assessment

To determine the signal and noise among the regions of interest (ROIs) in the obtained images, 6 ROIs were selected in each image, following Mraity Haab et al.'s [13], to determine the signal and noise of these regions. The first ROI was centered on the 5th lumbar vertebra (L5), the second on the right iliac crest, the third on the left iliac crest, the fourth on the right femoral neck, the fifth on the left femoral neck, and the sixth on the image's lateral edge, representing the background of the image with no specific anatomy. All ROIs were circular with the same area (13.684 mm²). Figure 4 represents the results of the ROIs obtained in each image using the ImageJ program.

Image 1

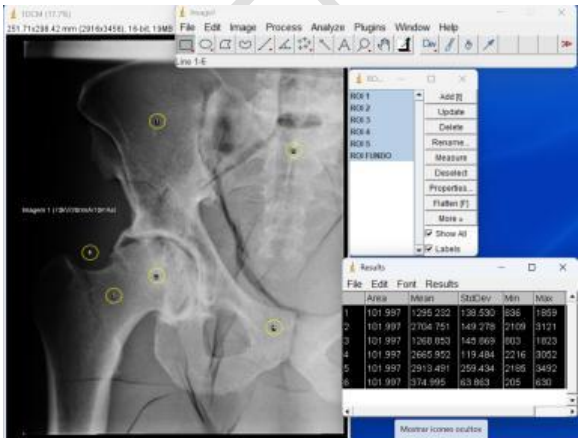

Image 2

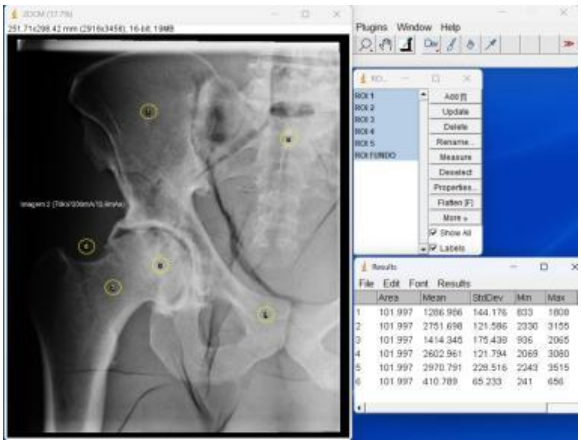

Image 3

Image 4

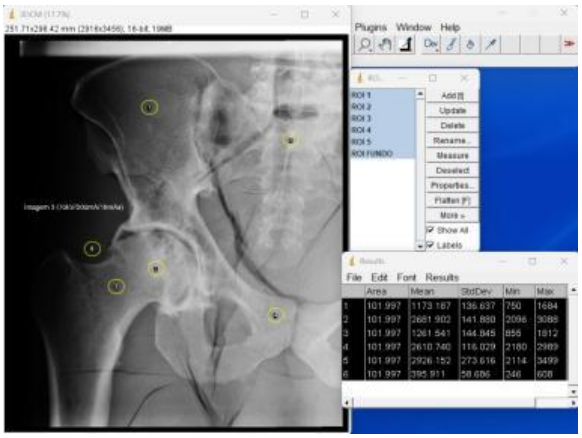

Image 5

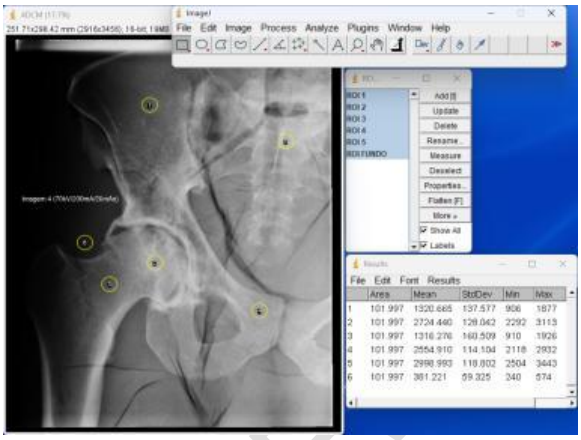

Image 6

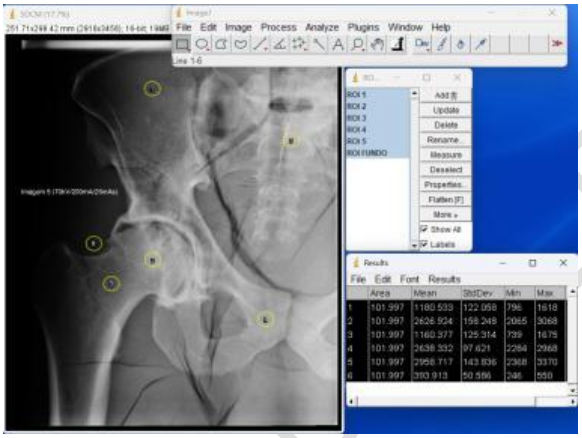

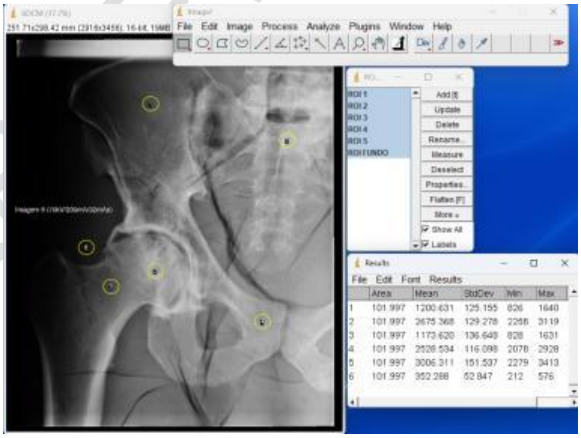

Fig. 4 - Results of average signal and noise values for each ROI obtained in the ImageJ program.
Source: Author's own.

Anatomical criteria established by the Commission of the European Communities for the hip examination/anatomy in the antero-posterior (AP) view include the visually sharp reproduction of the following structures: iliac bone, femoral head and neck (without strain or rotation), larger and smaller trochanters, standard cortex/trabecular patterns [14]. Table 3 represents the average signal and noise values obtained using the ROI tool in the ImageJ program.

Table 3 - Relates the ROIs and IQ descriptors.

		Image 1		Image 2		Image 3		Image 4		Image 5		Image 6	
ROI	**Anatomia**	**Signal**	**Noise**	**Signal**	**Noise**	**Signal**	**Noise**	**Signal**	**Noise**	**Signal**	**Noise**	**Signal**	**Noise**

1	**Iliac Wing (Right).**	1,295	139	1,287	144	1,173	137	1,321	138	1,181	122	1,201	125
2	**Femoral Head (Right).**	2,705	149	2,752	122	2,682	142	2,724	128	2,627	158	2,675	129
3	**Femoral Neck (Right).**	1,269	146	1,414	175	1,262	145	1,316	161	1,160	125	1,174	137
4	**Pubic Ramus**	2,666	119	2,603	122	2,611	116	2,555	114	2,638	98	2,529	116
5	**Sacrum**	2,913	259	2,971	229	2,926	274	2,999	119	2,959	144	3,006	152
6	**Background**	375	64	411	65	396	59	381	59	394	51	352	53

Source: Author's own.

The analysis of IQ Descriptors (Signal and Noise) for various Regions of Interest (ROI) in each image revealed a notable variation in values among different hip anatomical structures. The Signal, indicating the image signal intensity, exhibited subtle to significant variations in each ROI across all analyzed images. On the other hand, the Noise, representing interference or distortion in the image, also showed fluctuations, sometimes following patterns correlated with the Signal, other times varying more inconsistently.

The results among the evaluated images suggest that IQ differs among the examined anatomical structures. These variations could be attributed to differences in image acquisition or techniques used during the process. The importance of this analysis lies in the need to assess not only the overall image quality but also the specific quality in different anatomical areas. Understanding these variations can ensure better diagnostic accuracy and precise clinical interpretation of hip radiographic images, as different anatomical structures may require distinct technical considerations to optimize IQ.

For each image, the signal value (average of pixels) for each ROI and noise (respective standard deviation) for each examination/anatomy were evaluated. To better analyze IQ, the calculation of SNR was performed for each ROI/Anatomy, following equation 2.

$$SNR = \frac{Signal \quad Average \quad ROIs \quad 1;2;3;4\ e\ 5}{Background \quad Noise \quad ROI \quad 6} \tag{2}$$

To assess the influence of the technique on Radiographic Contrast (CR) of each image, the average signal difference of ROI 3 (right Femoral Neck) and ROI 6 (Background) was chosen, following equation 3.

$$CR = (ROI \quad 3) - (Background \quad) \tag{3}$$

Table 4 presents the average values of Signal-to-Noise Ratio (SNR) and Radiographic Contrast (CR) calculated by equations 2 and 3, respectively.

Table 4 - Summarizes the average values of SNR, CR.

	SNR	**D% SNR**	**CR**	**D%**	**ESAK (mGy)**	**D% ESAK**
Image 1	33,97	-15,20%	894	8,89%	2,08	-67,1%
Image 2	33,81	-15,60%	1004	22,29%	2,58	-59,2%
Image 3	36,31	-9,36%	866	5,48%	3,24	-48,7%

Image 4	36,8	-8,14%	935	13,89%	4,01	-36,6%
Image 5	23,34	-41,74%	766	-6,70%	4,96	-21,5%
Image 6	40,06	Reference	821	Reference	6,32	Reference

Source: Author's own.

According to Table 4, the highest Signal-to-Noise Ratio (SNR) value was for Image 6, followed by Image 4, 3, 2, and 1, as expected due to increased radiation dose.
Remarkably, Images 1, 2, 3, and 4 displayed SNR values of 15.20%, 15.60%, 9.36%, and 8.14%, respectively, lower compared to Image 6. However, they exhibited superior CR values of 8.89%, 22.29%, 5.48%, and 13.89%, respectively. Image 5 showed larger differences, with a 41.74% decrease in SNR and a 6.7% increase in CR, indicating a greater degradation of IQ that might affect the ability to differentiate areas of different densities in the image.
Surprisingly, despite the variations, Images 1, 2, 3, and 4 demonstrated lower ESAK values of 67.1%, 59.2%, 48.7%, and 36.6%, respectively, compared to Image 6, indicating a considerably high reduction in radiation exposure. These results suggest notable differences in IQ and radiation exposure among the analyzed images, emphasizing the importance of interpreting this data together to better understand its impact on clinical practice and patient safety.
It was observed that Radiographic Contrast (CR) showed little variation with the radiation dose. As outlined by Tompe; Sargar [15], CR can be conceptualized as a fractional disparity in the signal or brightness level manifested between the structure of interest and its surroundings. This contrast phenomenon is a result of the variation in X-ray absorption capacity by different anatomical tissues.

3.3 Dosimetry

As shown in Figure (2B), a total of 24 exposures were performed for each set of four measurements of Entrance Skin Air Kerma (ESAK) on the phantom's surface for each hip anatomy/examination. The mean value was calculated to reduce random error. Table 5 represents the ESAK readings obtained with the dosimetry system. The average values and their respective standard deviations (SD) were calculated.

Table 5 - Lists the dose readings for each obtained image.

Readings	**Image 1**	**Image 2**	**Image 3**	**Image 4**	**Image 5**	**Image 6**
	ESAK (mGy)					
R1	2,080	2,575	3,239	4,009	4,965	6,320
R2	2,089	2,579	3,235	4,009	4,963	6,327
R3	2,069	2,580	3,233	4,008	4,969	6,302
R4	2,075	2,577	3,249	4,008	4,960	6,318
Average R	2,078	2,578	3,239	4,009	4,964	6,317
DP	0,008	0,002	0,007	0,001	0,004	0,011

Source: Author's own.

The results reveal a consistent progression in radiation dose values as the images are sequentially acquired, showing a gradual increase in ESAK from Image 1 to Image 6. Although standard deviations are generally small, there's a slight increase in the deviation noted for Image 6, indicating possible variations in the recorded dose values. The percentage comparison with Image 6 demonstrates progressive reductions in dose values for the earlier images, suggesting optimizations in exposure techniques and possible adjustments to reduce applied radiation.
The constancy in the percentage deviation for Image 6 suggests consistency in the applied dose, possibly due to a specific exposure technique. These results are crucial for assessing and optimizing radiation exposure in medical procedures, seeking safer and more effective methods without compromising the quality of diagnostic images.

3.3 Figure of Merit

To verify how much loss of quality implies a reduction in dose, a Figure of Merit (FOM) was developed. The FOM quantifies the relationship between Image Quality (here taken as SNR) and the entrance surface dose (ESAK) and is applied to help gauge the influence of mA.s when considering both parameters simultaneously, as per Equation 4:

$$FOM = \frac{SNR}{ESAK} \quad (4)$$

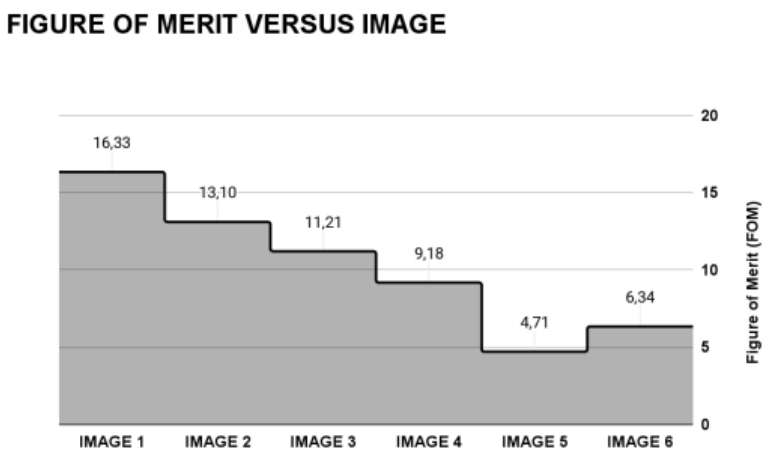

Fig. 5 - Results of the figure of merit (FOM)
Source: Author's own.

An interesting trend was observed by the Figure of Merit (FOM): as the FOM decreases, indicating a reduction in Image Quality (IQ) concerning radiation dose, the values decrease sequentially from Image 1 to Image 6.
Images 1, 2, and 3 display higher FOM, suggesting a better relationship between IQ and radiation dose, while images 4, 5, and 6 show lower FOM, indicating a less favorable relationship between IQ and dose. Image 5, in particular, demonstrates the lowest FOM, suggesting a potentially significant reduction in IQ concerning radiation dose.
Image 3, which exhibited the best cost-benefit relationship—i.e., dose versus IQ—was associated with the technique using 70 kVp with 16 mA.s, reducing the patient's dose by 48.7%, with a minor reduction in SNR, less than 10%, and an improvement in CR by 5.47%.

4. CONCLUSION

In this study, the exposure factors used in the hip examination service served as a reference (70kVp and 32 mA.s), represented by Image 6. A comparison of the obtained results for dose and Image Quality (IQ) reveals that, associated with the reduction in the product of current and exposure time (mA.s), more significant reductions in radiation dose concerning the impact on IQ were obtained. However, it was observed that Image 3, which showed the best cost-benefit relationship—i.e., dose versus IQ—was attributed to the technique using 70 kVp with 16 mA.s, reducing the ESAK by 48.7% (from 6.32 to 3.24) mGy, with a minor reduction in SNR, less than 10%, and an improvement in CR by 5.47%. These results emphasize the need for radiology professionals to seek imaging techniques that offer high diagnostic quality with the least possible patient exposure, prioritizing a safer and more effective radiology practice.

REFERENCES

1. Seeram, E., Davidson, R., Bushong, S., & Swan, H. (2013). Radiation dose optimization research: Exposure technique approaches in CR imaging–A literature review. Radiography, 19(4), 331-338.

2. Carroll, Q. B. (2023). Radiography in the Digital Age: Physics-exposure-radiation biology. Charles C Thomas Publisher.

3. Seeram, E., Davidson, R., Bushong, S., & Swan, H. (2016). Optimizing the exposure indicator as a dose management strategy in computed radiography. Radiologic technology, 87(4), 380-391.

4. Erenstein, H. G., Browne, D., Curtin, S., Dwyer, R. S., Higgins, R. N., Hommel, S. F., ... & England, A. (2020). The validity and reliability of the exposure index as a metric for estimating the radiation dose to the patient. Radiography, 26, S94-S99.

5. Furquim, T. A., & Costa, P. R. (2009). Garantia de qualidadeemradiologiadiagnóstica. Revista Brasileira de FísicaMédica, 3(1), 91-99.Bontrager, K. L., &Lampignano, J. P. (2015). Tratado de posicionamentoradiográfico e anatomiaassociada. Elsevier Brasil.

6. Broeke, J., Pérez, J. M. M., & Pascau, J. (2015). Image processing with ImageJ. Packt Publishing Ltd. Accessed on September 24, 2023.

7. Flintham, K., Alzyoud, K., England, A., Hogg, P., & Snaith, B. (2021). Comparing the supine and erect pelvis radiographic examinations: an evaluation of anatomy, image quality and radiation dose. The British Journal of Radiology, 94, 20210047.

8. Trozic, S., England, A., & Mekis, N. (2023). Erect pelvic radiography with fat tissue displacement: Impact on radiation dose and image quality. Radiography, 29(3), 546-551.

9. Yoneda, A., Fujii, H., & Tanaka, Y. (2023). Location of the ovaries in children and efficacy of gonadal shielding in hip and pelvis radiography. Journal of Orthopaedic Science, 28(5), 1165-1168.

10. Bontrager, K. L., &Lampignano, J. P. (2015). Tratado de posicionamentoradiográfico e anatomiaassociada. Elsevier Brasil.
11. Sandström, S., Pettersson, H., & Åkerman, K. (2003). The WHO manual of diagnostic imaging: radiographic technique and projections (Vol. 1). World Health Organization.

12. Möller, T. B., Reif, E., Stark, P., & Stark, P. (2000). Pocket atlas of radiographic anatomy (pp. 140-155). Thieme.

13. Mraity, H. A., England, A., Cassidy, S., Eachus, P., Dominguez, A., & Hogg, P. (2016). Development and validation of a visual grading scale for assessing image quality of AP pelvis radiographic images. The British Journal of Radiology, 89(1061), 20150430.

14. European Commission. European guidelines on quality criteria for diagnostic radiographic images. EUR 16260 EN. http://www.sprmn.pt/legislacao/ficheiros/European Guidelineseur16260.pdf. Published 1996. Accessed on September 24, 2023.

15. Tompe, A., &Sargar, K. (2020). X-Ray Image Quality Assurance.